CCFE
CULHAM CENTRE FOR FUSION ENERGY

UK Atomic Energy Authority

UKAEA-CCFE-PR(21)24

F. Schoofs, S. King, A. Cackett, M. Leyland, C. Hardie

Small Angle Neutron Scattering from CuCrZr coupons and components

Small Angle Neutron Scattering from CuCrZr coupons and components

F. Schoofs, S. King, A. Cackett, M. Leyland, C. Hardie

This is a preprint of a paper submitted for publication in IUCrJ

Small Angle Neutron Scattering from CuCrZr coupons and components

F. Schoofs[1], S. King[2], A. J. Cackett[1], M. Leyland[1], C. Hardie[1]

[1] United Kingdom Atomic Energy Authority, Culham Science Centre, Abingdon, OX14 3DB, United Kingdom

[2] ISIS Pulsed Neutron and Muon Source, Rutherford Appleton Laboratory, Harwell Campus, Didcot, OX11 0QX, United Kingdom

Abstract– Small Angle Neutron Scattering (SANS) is performed to analyse the microstructural state of reference CuCrZr material with carefully controlled heat treatments, small-scale manufacturing mock-ups of assemblies and high-heat-flux exposed mock-ups. The information derived from the SANS data corresponds well to existing literature data based on microscopic scale techniques. The manufacturing method as well as high-heat-flux testing conditions are confirmed to have little impact on the microstructural properties. The work also demonstrates that SANS can be used for millimetre-scale analysis of small engineering components with minimal surface preparation.

Keywords: - SANS; alloy; CuCrZr

1. Introduction

CuCrZr alloys are favoured in applications where a high thermal conductivity and high strength are required at elevated operating conditions, such as in heat exchange structures in nuclear fusion reactors, for example ITER and EU-DEMO (Kalinin & Matera, 1998; Kalinin *et al.*, 2007; Coenen *et al.*, 2016). Precipitation hardening, with precipitate dimensions in the 1-100 nm range, is crucial to their mechanical strength during operation and therefore needs to be extremely well controlled (Ivanov *et al.*, 2002; Cackett *et al.*, 2018). During manufacturing and use, these components are exposed to complex, non-uniform thermal cycles, which will impact on the CuCrZr microstructure. Atom probe tomography (APT) or transmission electron microscopy (TEM) provide direct visual information, but only on a very small sample (< 10 μm^3) (Chbihi *et al.*, 2012; Hatakeyama *et al.*, 2008; Jha *et al.*, 2021; Chen, Jiang, Jiang *et al.*, 2018; Edwards *et al.*, 2007). Small angle neutron scattering (SANS), on the other hand, is able to provide a bulk statistical measurement on millimetre-scale samples, while maintaining the sensitivity for the precipitate dimensions (Schmidt, 1991; Vogel, 2013). Here, we compare SANS data for different ageing conditions of a CuCrZr alloy in small samples as well as in bulk

components exposed to different temperature cycles as part of the EU-DEMO "thermal break" divertor exhaust mock-up development process (Barrett *et al.*, 2015; You *et al.*, 2018; Fursdon *et al.*, 2017; Lukenskas *et al.*, 2019).

2. Experimental

2.1. Materials

In this work we discuss three different sample sets: reference coupons of CuCrZr with controlled heat treatment; CuCrZr pipes with a single block of W brazed to it, used as manufacturing mock-ups (MUPs) and CuCrZr pipes with multiple W blocks brazed to it which have been exposed to high-heat fluxes. In all cases the starting material was a solution annealed CuCrZr alloy (CuCrZr 2.1293, Zollern GmbH & Co. KG), with a composition of 1 wt% Cr, 0.06 wt% Zr and a P content of less than 0.005 wt%. The average grain size in the as-received state is 77.9 μm.

2.1.1. Reference coupons

Sections of the starting material were heat treated in vacuum for 2 hours at 400 °C, 480 °C, 550 °C, 600 °C, 650 °C and 700 °C. The 480 °C condition corresponds to the optimal ageing time and temperature for this alloy (Merola *et al.*, 2002; Kalinin *et al.*, 2007). Material coupons of 15 x 15 x 1 mm^3 were cut for all heat treatments, as well as 0.5 and 1.5 mm thick samples of the as-received and 700 °C treatment. The data on the latter samples is not shown here, but no thickness effects on the SANS data were observed, i.e. 0.5, 1 and 1.5 mm samples all produced the same integrated 1D SANS data when normalised for the thickness.

2.1.2. Manufacturing mock-ups (MUP)

A single rolled tungsten block, with dimensions 12 x 23 x 30 mm and a central bore of 19 mm, containing a 1 mm cast Cu interlayer (ALMT, Japan) was vacuum brazed using an Au-Cu braze to a 15 mm diameter, 1.5 mm thick CuCrZr pipe as previously described (Lukenskas *et al.*, 2019). The brazing cycle for the MUPs is shown in Fig. 1b – the difference between MUPs A and B is that the CuCrZr pipe in "B" has undergone this cycle twice, to improve braze flow and adhesion after removal of the segregated Zr at the surface, based on prior experience at UKAEA with brazing this alloy.

The MUPs were cut lengthwise by wire-EDM to expose the pipe cross-section. An additional cut was made to remove the tungsten and expose the Cu interlayer. The remaining Cu thickness was measured to account for it in the SANS data reduction. No further sample preparation was done on the SANS samples. On each MUP, 4 measurement locations were

investigated: 2 on the pipe away from and 2 underneath the tungsten monoblock (see Figure 2). SANS measurements were taken with a 2 x 5 mm beam, with the shorter dimension aligned along the pipe axis.

2.1.3. High-heat-flux exposed pipes

Thermal break divertor mock-ups containing 4 tungsten tiles were manufactured and subsequently exposed to high heat flux conditions in the GLADIS test facility, while being actively cooled with pressurised water at 130 ºC (Lukenskas *et al.*, 2019; Greuner *et al.*, 2019). The heat flux in this facility is delivered by a hydrogen ion beam. Specifically, the following components were obtained: CCFE#7 (exposed to 25 MW/m^2 + 100 cycles at 10 MW/m^2, then 35 MW/m^2 + 100 cycles at 25 MW/m^2) and CCFE#8 (exposed to 25 MW/m^2 + 100 cycles at 10 MW/m^2). These components were sectioned longitudinally and from one half, the tungsten was wire-cut away to retain only the CuCrZr pipe and a minimal amount of braze/interlayer. The thickness of each section was measured to account for it in the SANS data reduction.

In addition to these samples a piece of pipe, well away from the tungsten blocks, which had just been exposed to the brazing cycle, was measured at the same time. This sample is referred to as the 'reference pipe'.

2.2. Small Angle Neutron Scattering

Small Angle Neutron Scattering (SANS) was performed at the ISIS Pulsed Neutron & Muon Source (https://wwww.isis.stfc.ac.uk/, Didcot, UK) (Melnichenko, 2016; Heenan *et al.*, 2011).

Data were collected on the SANS2D (reference coupons) and ZOOM (MUPs and pipe section) instruments, respectively, in transmission geometry (i.e. with the neutron beam normal to the sample). In this geometry, the SANS data are generally insensitive to any surface layer contributions (e.g. oxide layers, surface roughness) extending less than ~1000 Å. The beam footprint at the sample was collimated to 8 mm diameter on the reference coupons and 5 mm high by 2 mm wide on the MUPs and pipe sections, using cadmium masks located as close as possible to the samples. In the case of the MUPs, the long axis of the beam footprint was aligned across the diameter of the tube (see Figure 2a), whereas in the case of the pipe sections it was aligned along the length of the tubes to allow measurements alongside either the top or bottom edge of the original component (by rotating the pipe sections ± 45° into normal incidence) as well as through the centre (see Figure 2c).

SANS2D and ZOOM are time-of-flight instruments, which means they utilise a range of neutron wavelengths (1.75 – 16.5 Å) to simultaneously probe a very broad range of *d*-spacing (for the instrument configuration used, 8 – 3140 Å), and are thus ideal for the type of study

performed here. However, examination of the transmission data revealed prominent Bragg 'edges' at wavelengths shorter than 4.3 Å, a common occurrence in multi-phasic materials with crystalline regions, and so these wavelengths were excluded during the data reduction. In the figures below, the *d*-spacing is expressed as the (magnitude of) the scattering vector, Q ($= 2\pi/d = 4\pi \sin\theta/\lambda$, where λ is the neutron wavelength and 2θ is the scattering angle). On an accelerator source like ISIS, the neutron flux is proportional to the time integrated current arising from the protons striking the metal target. Scattering data were accumulated for between 20-80 μAhr (~0.5-2hrs) and transmission data for 6-8 μAhr.

For SANS to arise, there must be a contrast – a difference in scattering length density (SLD) – between sample components. The SLDs of Cr (3.01×10^{-6} Å^{-2}) and Zr (3.07×10^{-6} Å^{-2}) are so similar that the neutrons are unable to distinguish between Cr- and Zr-rich precipitates or phases. But it is likely that the dominant precipitate phase is a Cr-rich phase, especially given the low Zr content (Chen, Jiang, Jiang *et al.*, 2018; Abib *et al.*, 2019). Instead, here SANS arises from the contrast between Cr and Zr containing precipitates and a predominantly Cu matrix (SLD 6.55×10^{-6} Å^{-2}). We note that the SLD of W is also 3.01×10^{-6} Å^{-2} and thus any residual scattering from the remains of the W monoblock would be indistinguishable from the Cr or Zr containing precipitates. Where the residual W can have an effect, is through neutron absorption as it has the largest absorption cross-section of the four nuclei at 18.3 barns (Cr: 3.0 barns; Zr: 0.2 barns; Cu:3.8 barns). But for comparison, note that the equivalent value for Cd – used in neutron shielding/masking – is 2520. The measured SANS intensities, *I(0)*, were placed on an absolute scale by reference to the scattering from a standard sample of known *I(0)* measured with the same instrument setup.

Data reduction was performed using the Mantid framework (Mantid Project, 2013; Arnold *et al.*, 2014) in accordance with standard procedures for SANS2D and ZOOM. During processing, the data from the 2D detectors were radially-averaged to 1D. The data were also normalised to an effective sample thickness (i.e. pathlength). The curvature of the surfaces is not taken into account during the data reduction: as the neutron beam was symmetrically incident across the diameter of the MUP and the detector was 4 m behind the sample, it is a reasonable approximation to assume that the pipe surface is flat.

The reduced data were primarily fitted to a scattering function consisting of a combination of Porod's law (Schmidt, 1991) and a single Lorentzian peak, as a function of the scattering vector Q:

$$I(Q) = AQ^{-\alpha} + \frac{B}{1+(L*|Q-Q_{peak}|)^2} + C \quad (1)$$

Where α (the Porod exponent) is related to the degree of interfacial roughness, L (an Ornstein-Zernicke-like correlation length) is related to the radius of the precipitates, Q_{peak} (the peak position) is related to the separation between precipitates, A and B are scale factors and C is the Q-independent background. The advantage of this function is it does not presuppose a uniform shape for the precipitates (e.g. spheres) as others studying these alloys have done (Abib *et al.*, 2019), nor does it infer a mechanism for the phase separation (i.e. nucleation and growth *vs* spinodal decomposition). However, as morphological changes in the precipitates were evident, some of the same data were also fitted to scattering functions where the Lorentzian term in Equation 1 was replaced by the form factors for homogeneous spheres or ellipsoids:

$$I(Q) = AQ^{-\alpha} + B(\Delta_{SLD})^2\langle F^2(Q,r)\rangle + C \quad (2)$$

Where the angle brackets denote an orientational average, $F(Q,r)$ is the scattering amplitude and r is the form radius ($r = r_{sphere}$ or $r_{ellipsoid}$):

$$F(Q,r) = \frac{3(\mathrm{Sin}\, Qr - Qr\, Cos\, Qr)}{(Qr)^3} \quad (3)$$

$$r_{ellipsoid} = R_{equ}\left[1 + Sin^2\varphi\left(R_{pol}^2/R_{equ}^2 - 1\right)\right]^{1/2} \quad (4)$$

Where R_{equ} and R_{pol} are the equatorial and polar radii of the ellipsoid, respectively, and ϕ (over which the averaging is performed) is the angle between the rotational axis of the ellipsoid and $\bar{Q}$. The ellipsoid is oblate if $R_{pol} < R_{equ}$ and prolate if $R_{pol} > R_{equ}$. In practice, an integration over a range of r was also performed (using a lognormal distribution) to allow for the effect of size dispersity. This model-fitting was performed using the SasView software (version 5.0.4, https://www.sasview.org/). Further details of the models can be found in its comprehensive help documentation. The average precipitate spacing in the ellipsoid model has been estimated as:

$$spacing = \left(\frac{B}{\frac{4}{3}\pi R_{equ}R_{pol}^2}\right)^{-1/3} \quad (5)$$

which is valid when the scale factor $B >> A$ in equation (2) under which condition B is approximately equivalent to the volume fraction of precipitates.

3. Results & discussion

3.1. Reference coupons

Figure 3 shows the 2D scattering intensity against Q_x and Q_y for 3 different conditions, namely as-received (solution annealed), 480 °C and 550 °C. As expected a spherically symmetric pattern dominates the scattering – except for the optimally aged sample (Figure 3b).

This scattering profile is slightly elongated in the Q_y direction. Rotating the sample by 90° in the beam and remeasuring did indeed rotate the pattern as well, indicating that the precipitates in this CuCrZr coupon have some preferential alignment (along Q_x in the figure). Since this anisotropy occurs only at the peak-aged condition, it might be related to the β'(II) precipitates, which are an intermediate between the initially formed β'(I) and the β precipitates characteristic of over-ageing as defined and observed by (Chen, Jiang, Jiang *et al.*, 2018).

For the 1D data reduction of this anisotropic profile, only the data within an azimuthal range extending ± 30° either side of the meridian was used. An overview of the 1D intensity versus scattering data for all temperature conditions is shown in Figure 4. There is a clear trend, consistent with the heat treatment of each sample. No distinct peak or characteristic features are present in the solution annealed sample. After the 400 °C treatment, a peak starts to emerge, becoming more pronounced after the 480 °C treatment. Ageing at higher temperatures shifts this feature to lower Q values (longer length scales). After ageing at 650-700 °C, a second peak emerges at higher Q than the first one.

Fitting these 1D spectra with equation (1) where possible (see Figure 5), shows a variation of the precipitate interface, based on the Porod exponent (Table 1). An α value of 4 indicates a perfectly smooth interface, whereas a value of 3 indicates a much rougher interface (Schmidt, 1991; Teixeira, 1988). Initially the precipitates are coherent with the matrix (Porod exponent close to ideal, i.e. 4), but become incoherent with over-ageing and thus tend towards 3. This has been independently observed by TEM on peak-aged and over-aged samples (Batra *et al.*, 2003; Chen, Jiang, Jiang *et al.*, 2018; Chen, Jiang, Liu *et al.*, 2018; Jha *et al.*, 2021). Note that coherent and incoherent here refer to the condition of the precipitate interface, not the type of neutron-nucleus interaction.

Equation (1) produces a poor fit for the reference squares annealed at 650 °C and 700 °C. These data are more cogently reproduced by the ellipsoid model in equations (2)-(4). This corresponds to the findings from TEM and APT data which indicate aligned, elongated precipitates upon overaging (Chbihi *et al.*, 2012; Chen, Jiang, Jiang *et al.*, 2018; Cackett, 2020; Jha *et al.*, 2021). The SANS data seem to support a gradual morphological evolution from spherical precipitates at or below peak-aging, to *oblate* ellipsoidal precipitates (axial ratio ~1:2) at 600 °C, to more rod-like precipitates (axial ratio ~1:12) at 700 °C. The apparent second peak in the SANS at these higher temperatures is in fact a consequence of the oscillatory nature of the ellipsoidal scattering function. It is to be noted that all of our model-fitting indicates really quite broad precipitate size distributions (e.g. 25~60 % of the median radius).

Table 1 shows a comparison of the fitting parameters extracted from SANS, with data from TEM on sister samples that have undergone exactly the same heat treatment (Cackett *et al.*, 2018) as well as other TEM and APT data from literature (Chbihi *et al.*, 2012; Chen, Jiang, Jiang *et al.*, 2018). The precipitate sizes are well correlated between SANS and TEM/APT, at least for the under-aged or peak-aged samples. They also correspond well with those determined from other SANS studies on a CuCrZr alloy of similar composition, which extracted a spherical diameter of 3.2 nm in samples annealed at 550 ºC for 4 hours (Abib *et al.*, 2019). The separation distance (related to the number density of precipitates) shows a better correspondence at higher temperatures, although for the case of TEM these are often an estimate based on the specimen thicknesses in a particular sample region, whereas SANS provides a mm-scale overview through the sample thickness. As the temperature and amount of over-aging increases, especially on the 650 ºC and 700 ºC samples, the quality of the fit with a single Lorentzian peak deteriorates, suggesting that this model is no longer appropriate. This could be due to multiple types of scatterers/precipitates and/or their shape becoming more pronounced, as observed by (Chbihi *et al.*, 2012; Jha *et al.*, 2021) and discussed above.

These experiments on carefully controlled samples demonstrate that SANS can clearly distinguish between different CuCrZr heat treatments, with an interpretation of the results comparable to TEM and APT. Similar conclusions were drawn for FeCr phase separation data (Xu *et al.*, 2016).

3.2. Manufacturing mock-ups

Figure 6 shows the SANS data for the 4 different measurement points on MUP A, which should be comparable to the 480 °C coupon sample. The derived parameters of fitting equation (1) to the data from MUP A and MUP B are shown graphically in Figure 7.

The values for the Porod exponent and precipitate diameter on the copper pipe on either side of the tungsten block are broadly in line with the values for the peak-aged reference samples in Section 3.1 and Table 1, with the precipitate spacing being slightly smaller. There appears to be a slight variation in all 3 parameters under the tungsten block, consistent with the trend on over-ageing from Section 3.2. The variation in precipitate size (Figure 7c) is around 1 or 2 times the lattice constant of crystalline copper, so it is significant. This would be consistent with a subtly different thermal response of the CuCrZr due to the locally different thermal mass, resulting in

a slower cooling rate after the solution annealing, which promotes the nucleation of secondary phases (Park *et al.*, 2008).

These experiments confirm that the brazing cycle heat treatment from Figure 1b does indeed produce near-optimum properties in the CuCrZr, with limited difference whether the pipe goes through one or two braze heat treatment cycles. There is however a slight over-ageing present under the tungsten blocks.

3.3. High-heat-flux exposed pipes

The results of fitting the SANS data for the reference pipe and high-heat-flux exposed pipes are shown in Figure 8. In the case of the reference pipe, all physical parameters should be the same regardless of the pipe orientation (i.e. left edge, right edge or centre), so the spread on this measurement gives an indication of the precision of both the measurement and the fitting procedure. For the Porod exponent and precipitate spacing the values are close together, whereas there is a ~0.25 nm difference on the fitted precipitate diameter between the right-hand side and the left & centre values. This is just below the difference observed in Section 3.2 under the tungsten block and around the value of the lattice constant of copper, so it could be a real, local deviation.

For the high-heat-flux exposed samples, there does not appear to be a distinct trend between the top or front (exposed to the high heat flux) and the bottom or back (not facing the particle beam). This is in line with the expectation from Finite Element Analysis modelling, showing that the temperature at the top of the pipe remains below 360 °C even when loaded to 20 MW/m^2, while the bottom of the pipe remains at the coolant temperature of 130 °C (Domptail *et al.*, 2020). At this temperature, no changes to the precipitates are anticipated (Kalinin *et al.*, 2007). Only the Porod exponent appears to be different between top & bottom away from the tungsten blocks, with the exponent from the heat-exposed side corresponding well with the values found in coupons aged at a similar temperature and the reference pipe.

These data, combined with the reference pipe data, imply that there is no meaningful temperature difference between the front and back of the MUPs during high heat flux exposure in the GLADIS facility and that the mechanical properties in the as-fabricated state remain more or less intact under these operating conditions. This demonstrates that the thermal break concept and its manufacturing route produce and retain the optimum CuCrZr structure.

4. Conclusion

In summary, we have demonstrated that SANS can be used to resolve the state of CuCrZr

precipitates in fusion reactor divertor components at a gauge volume of millimeter scale, with minimal sample preparation required. On reference samples with different heat treatments, there is good correspondence with APT and TEM data.

The manufacturing method for the thermal break EU divertor concept studied here, namely brazing the solution annealed CuCrZr pipe, followed by a gas quench and an ageing treatment, is demonstrated to give near-optimal mechanical properties, with variations underneath the tungsten monoblock, as detected by SANS, suggesting slight over-ageing. The near-doubling of the precipitate spacing would roughly halve the component of the strength offered by the precipitates, though the error bars on these numbers are large.

Importantly, there was no significant variation or deterioration of the microstructure observed in high-heat-flux exposed samples, confirming that the mechanical properties of as-manufactured divertors can be assumed to remain valid under standard operating conditions.
The sensitivity of SANS for precipitate coherency with the matrix shows promise to investigate neutron-irradiated samples over millimetre-scale, to aid in elucidating the irradiation-induced hardening and softening behaviour.

(a) 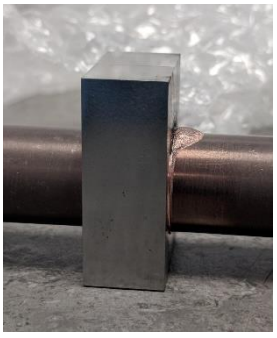 (b) 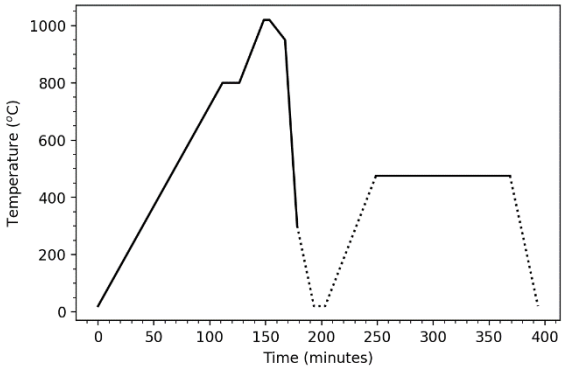

Figure 1 (a) Photo of MUP B after brazing and before sample preparation, showing the CuCrZr tube passing through a W monoblock. (b) Furnace cycle for the MUPs.

(a) 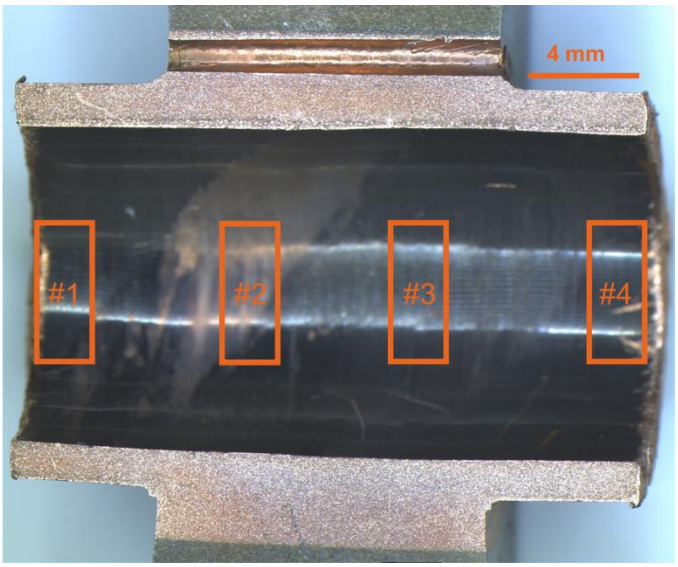

(b) 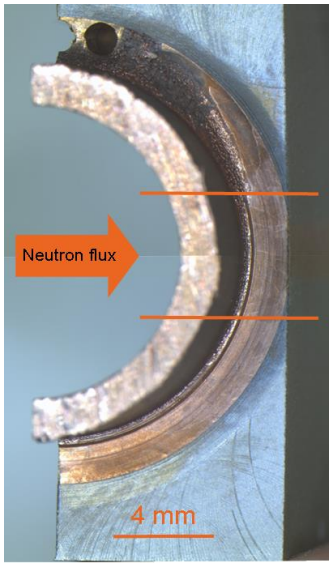

(c) 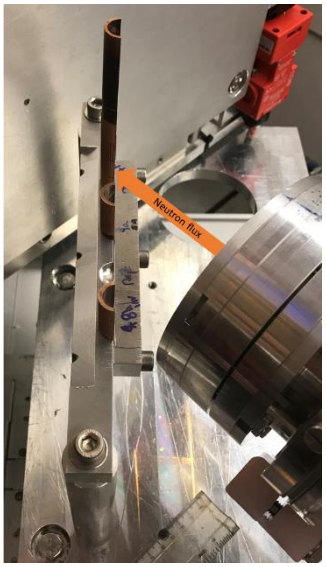

Figure 2 (a) Cross-section of MUP B, with the SANS (2 x 5 mm rectangles) measurement positions indicated. (b) Side view of MUP B showing the SANS measurement positions with the 5 mm high beam. (c) View of the pipe sections installed on the ZOOM instrument. The steel safety shutter behind the samples is raised during the measurements. The samples could be rotated and translated in the neutron beam. In the image the right-hand edge of the right-hand pipe section has been rotated into normal incidence to the incoming neutron beam.

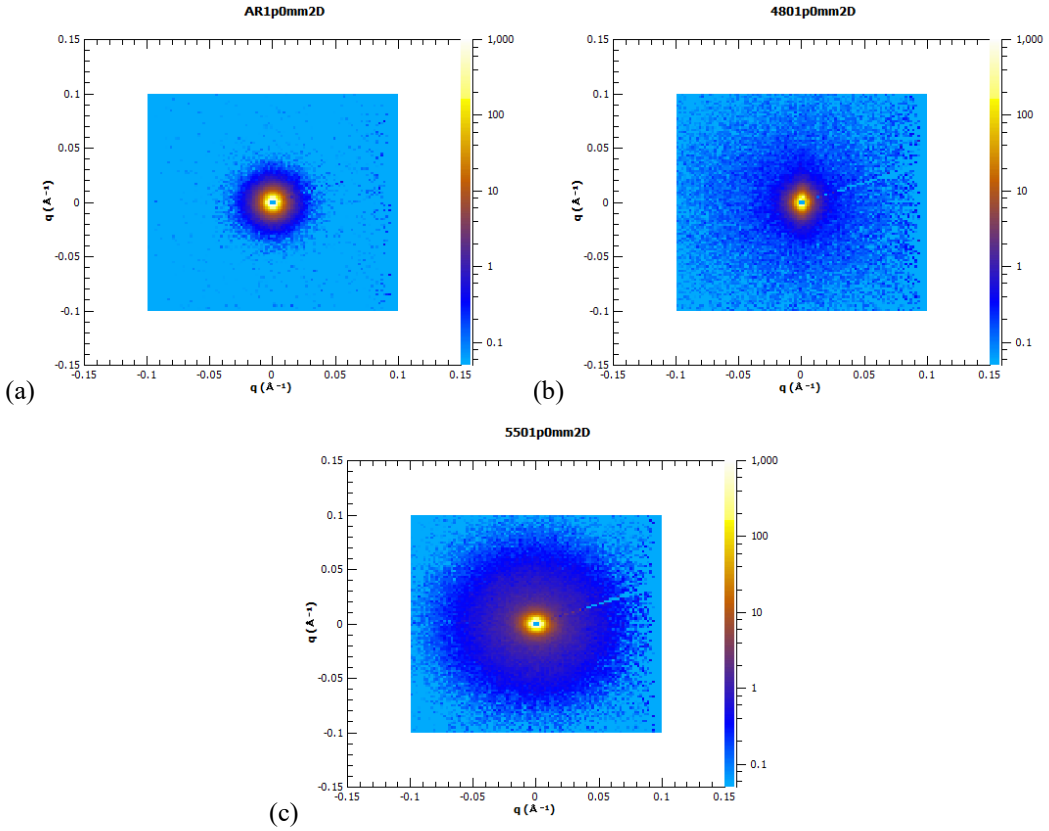

Figure 3 Two-dimensional scattering patterns for the (a) solution annealed; (b) 480 °C aged; (c) 550 °C aged samples. All three plots have the same axes and scales. Note the slight longitudinal anisotropy present in (b).

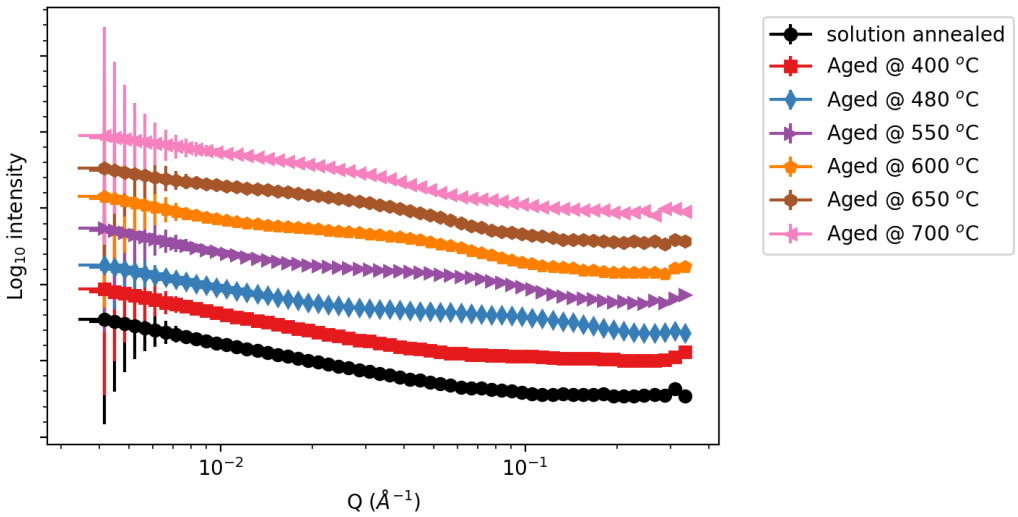

Figure 4 Radially integrated SANS data measured on SANS2D from the reference coupons for all heat treatment conditions, showing the evolution of nanostructure in the alloy. The data are offset vertically for clarity.

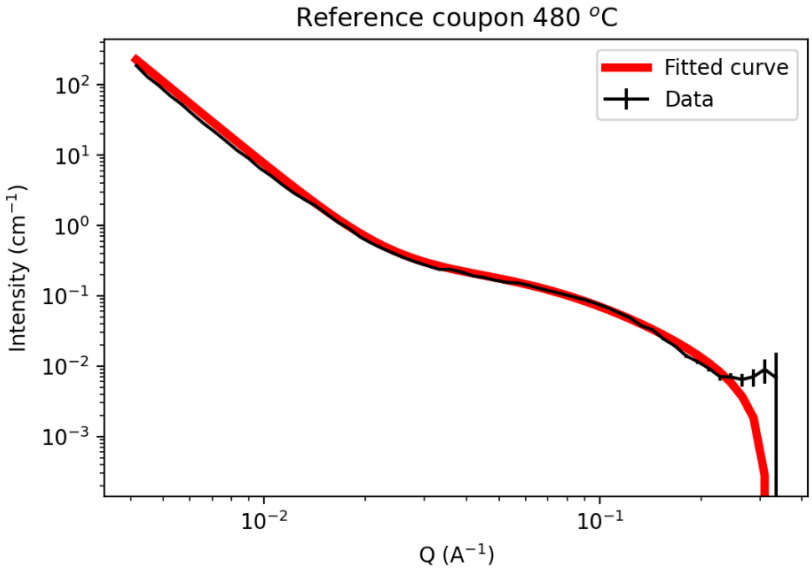

(a)

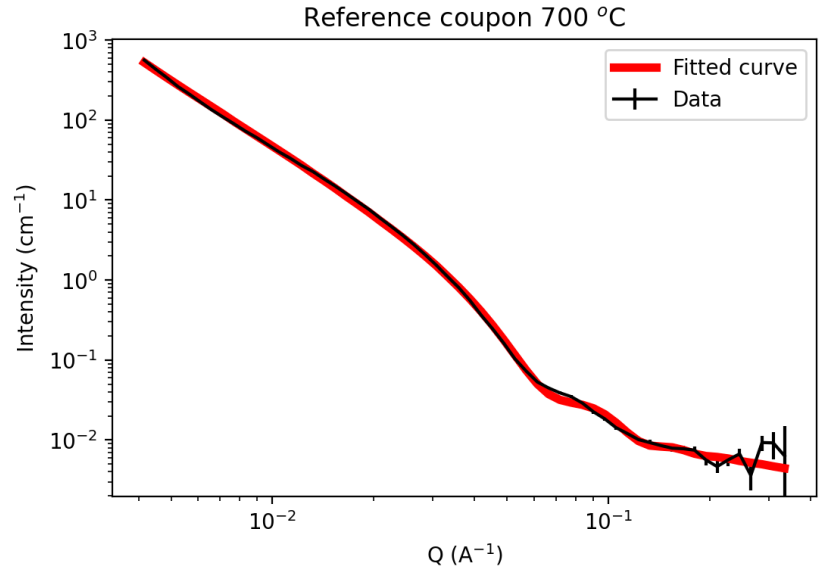

(b)

Figure 5 Examples of model-fitting of the SANS data from the reference coupons: (a) 480 °C annealed sample fitted to Equation (1); (b) 700 °C annealed sample fitted to Equations (2)-(4).

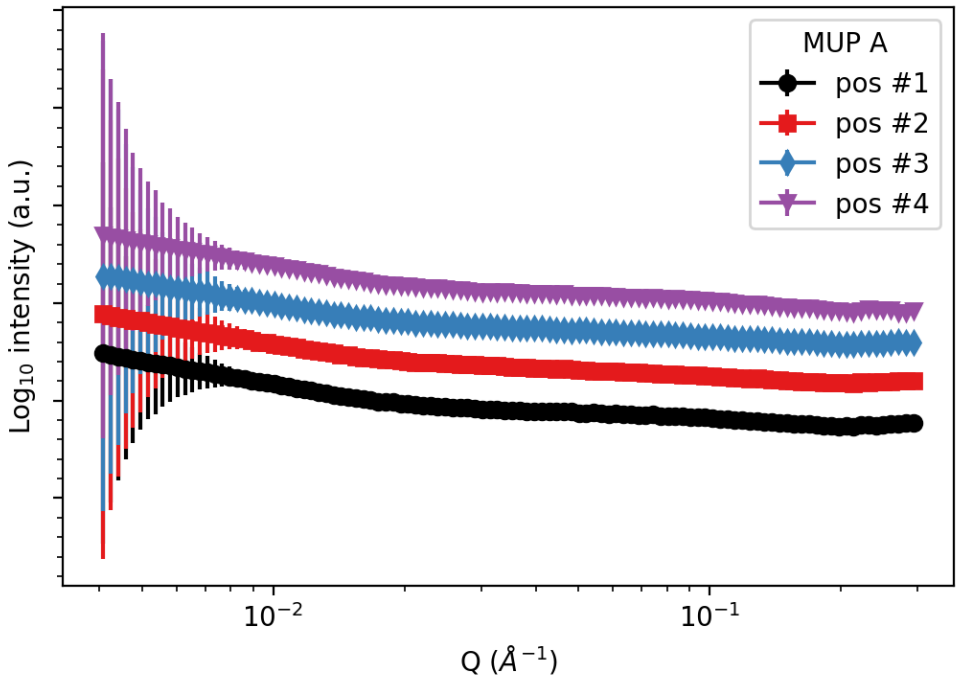

Figure 6 Radially integrated SANS data measured on ZOOM at the four positions on MUP A (see Figure 2a for locations). The data are offset vertically for clarity.

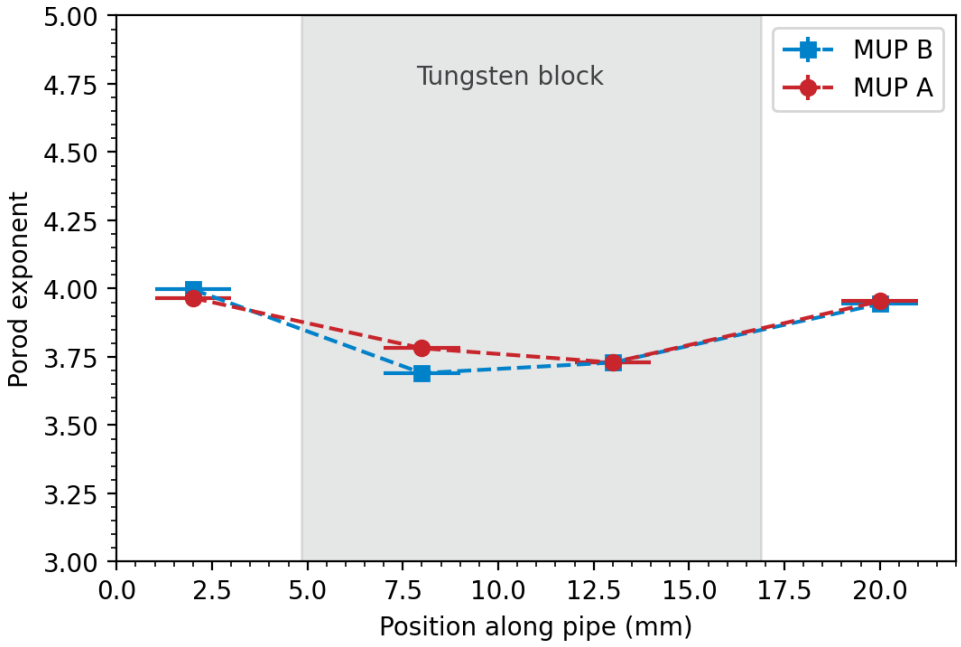
Tungsten block
MUP B
MUP A
Porod exponent
Position along pipe (mm)
5.00
4.75
4.50
4.25
4.00
3.75
3.50
3.25
3.00
0.0
2.5
5.0
7.5
10.0
12.5
15.0
17.5
20.0

(a)

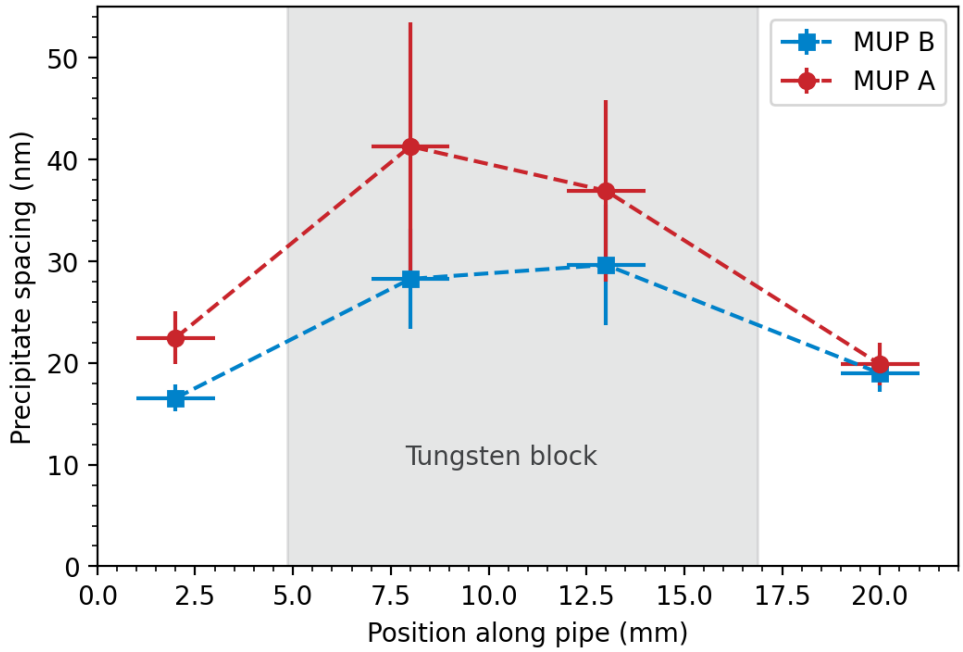
Tungsten block
MUP B
MUP A
Precipitate spacing (nm)
Position along pipe (mm)
50
40
30
20
10
0
0.0
2.5
5.0
7.5
10.0
12.5
15.0
17.5
20.0

(b)

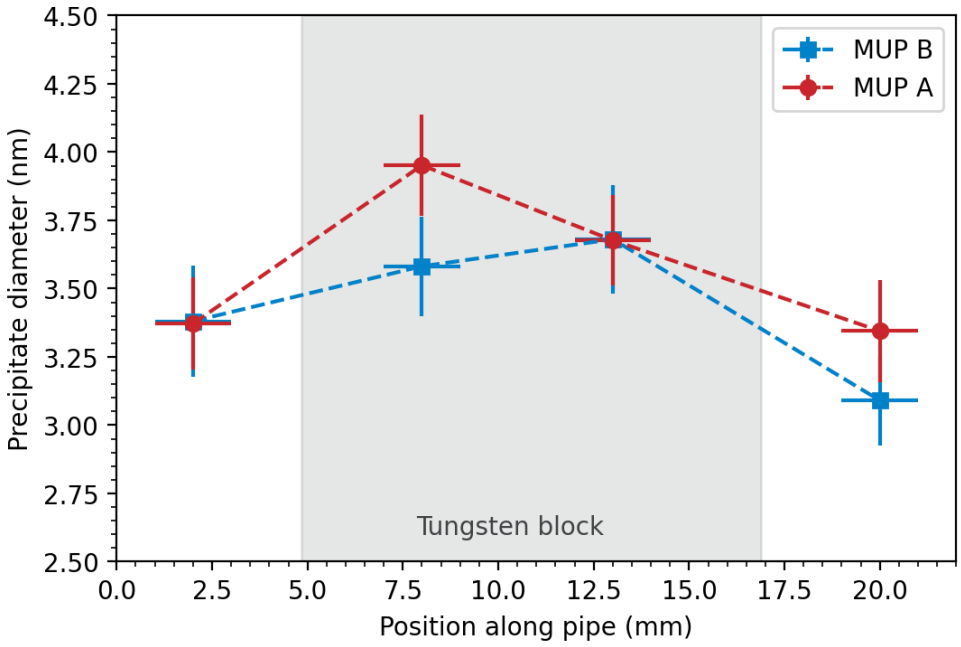

(c)

Figure 7 Parameters extracted from fitting SANS data from the four measurement areas on MUP A and MUP B to Equation (1): (a) Porod exponent; (b) Precipitate spacing; (c) Precipitate diameter. The horizontal error bars reflect the width of the beam. The vertical error bars represent one standard deviation on the parameters as derived from the model fit. The position of the tungsten block is marked by a grey rectangle.

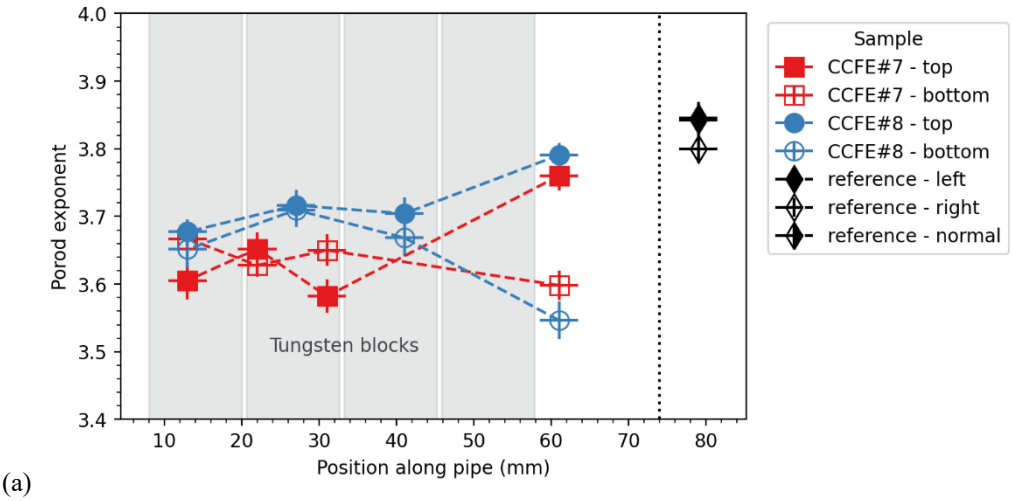

(a)

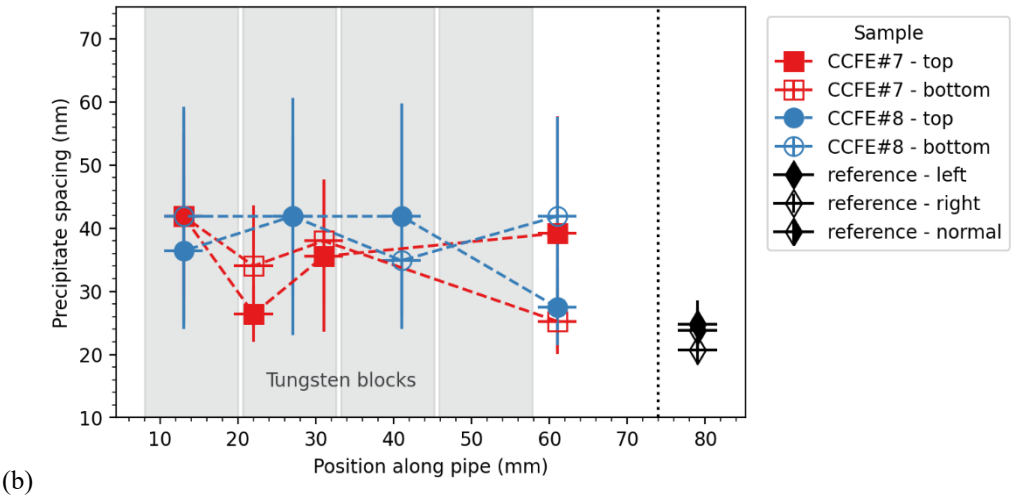

(b)

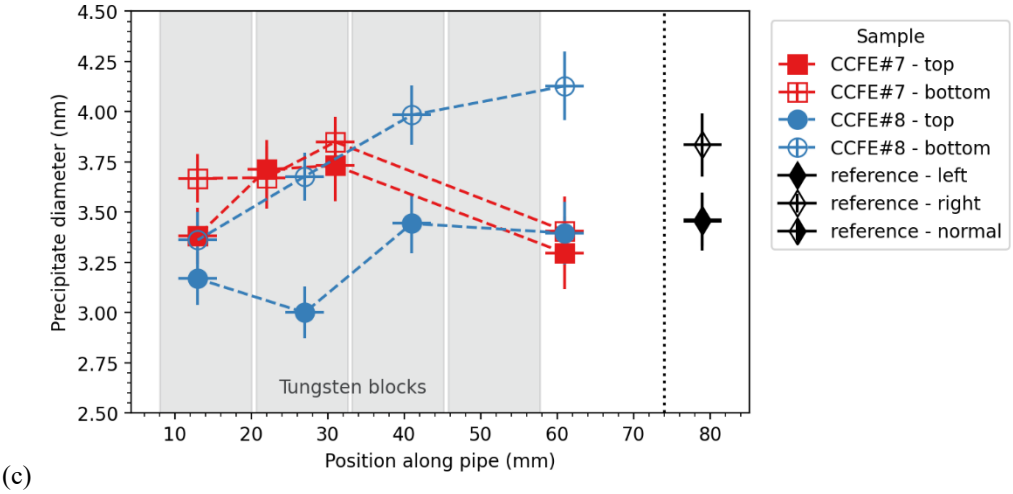

(c)

Figure 8 Parameters extracted from fitting the SANS data from the high heat flux exposed samples & reference pipe: (a) Porod exponent; (b) Precipitate spacing; (c) Precipitate diameter. The horizontal error bars reflect the width of the beam. The vertical error bars represent one standard deviation on the parameters as derived from the model fit. The reference data in all 3 orientations are plotted on the same x-axis scale for comparison. Filled symbols refer to the heat flux exposed top surface; open

symbols refer to the bottom of the MUP pipe samples. The positions of the tungsten blocks are marked by grey rectangles.

Table 1 Comparison of SANS data with TEM and APT data on precipitate diameter & spacing. The average spacing was derived from the APT or TEM precipitate density n as $n^{-1/3}$. The SANS fitting model is denoted by L = Lorentzian, S = sphere and E = ellipsoid. Note that the fit of the Lorentzian model is particularly poor for the 600 ºC, 650 ºC and 700 ºC data, so these values are given in brackets. The ellipsoid model for the 700 ºC data does not allow the calculation of the precipitate spacing, because the condition B >> A in equation (2) is not valid.

Material condition	SANS fitting model	SANS Porod exponent	SANS precipitate diameter (nm)	SANS precipitate spacing (nm)	TEM/APT precipitate diameter (nm)	TEM/APT precipitate spacing (nm)	Reference
As received	L	3.83 ± 0.005	N/A	N/A	N/A	N/A	SANS: this work; TEM:
2 hr aged 400 °C	L	3.89 ± 0.006	1.11 ± 0.11	N/A	1.56	N/A	(Cackett *et al.*, 2018; Cackett,
2 hr aged 480 °C	L	3.91 ± 0.02	3.27 ± 0.13	35.81 ± 3.06	3.18	13.3	2020; Cackett *et al.*, 2021)
	S	3.67 ± 0.01	2.40 ± 0.22				
2 hr aged 550 °C	L	3.84 ± 0.94	10.31 ± 0.05	20.26 ± 0.08	7.04	20.7	
2 hr aged 600 °C	L	3.58 ± 0.008	20.90 ± 0.07	28.09 ± 0.06	12.02	37.9	
	S	4.18 ± 0.01	7.70 ± 0.22				
	E	4.18 ± 0.01	6.92 x 14.28	84.0			
2 hr aged 650 °C	L	(3.07 ± 0.01)	(39.95 ±0.16)	(39.44 ± 0.07)	15.99	60.0	
	E	3.22 ± 0.02	10.53 x 23.05	144.8			
2 hr aged 700 °C	L	(3.28 ± 0.01)	(152.42±4.50)	(44.10 ± 0.1)	33.17	104.4	
	E	2.63 ± 0.01	0.87 x 10.08				
5 hr aged 440 °C		-	-	-	-	9.52 ± 0.25	(Chbihi *et al.*, 2012)
10 hr aged 440 °C		-	-	-	-	15.47 ± 0.77	
2 hr aged 450 °C		-	-	-	4	-	(Chen, Jiang, Jiang *et al.*, 2018)
Prime Aged (PA)		-	-	-	-	15.7	(Edwards *et al.*, 2007)
PA + 600 °C/2 hr		-	-	-	-	38.2	
PA + 700 °C/4 hr		-	-	-	-	87.4	
3 hr aged 460 °C		-	-	-	2.2-2.8	15.7-17.1	(Hatakeyama *et al.*, 2008)
reference		~4	2.2 ± 0.4				(Abib *et al.*, 2019)
ECAP + 4 h 550 °C		~4	3.2 ± 1.0	11.6	2.5	7.09	

Funding information. This work has been funded by the UK Government Department for Business, Energy & Industrial Strategy and the RCUK Energy Programme [grant number EP/T012250/1].

Acknowledgements - We thank the Science & Technology Facilities Council and the ISIS Pulsed Neutron & Muon Source for neutron beamtime on LOQ (RB1790202; DOI: 10.5286/ISIS.E.RB1790202), SANS2D (RB1800098; DOI: 10.5286/ISIS.E.RB1900098) and

ZOOM (RB1920008; DOI: 10.5286/ISIS.E.RB1920008). This work benefited from the use of the SasView application, originally developed under NSF award DMR-0520547. SasView also contains code developed with funding from the European Union's Horizon 2020 research and innovation programme under the SINE2020 project, grant agreement No 654000. To obtain further information on the data and models underlying this paper please contact PublicationsManager@ukaea.uk.

References

Abib, K., Azzeddine, H., Alili, B., Lityńska-Dobrzyńska, L., Helbert, A. L., Baudin, T., Jegou, P., Mathon, M. H., Zieba, P. & Bradai, D. (2019). *Kov. Mater.* **57**, 121–129.

Arnold, O., Bilheux, J. C., Borreguero, J. M., Buts, A., Campbell, S. I., Chapon, L., Doucet, M., Draper, N., Ferraz Leal, R., Gigg, M. A., Lynch, V. E., Markvardsen, A., Mikkelson, D. J., Mikkelson, R. L., Miller, R., Palmen, K., Parker, P., Passos, G., Perring, T. G., Peterson, P. F., Ren, S., Reuter, M. A., Savici, A. T., Taylor, J. W., Taylor, R. J., Tolchenov, R., Zhou, W. & Zikovsky, J. (2014). *Nucl. Instruments Methods Phys. Res. Sect. A Accel. Spectrometers, Detect. Assoc. Equip.* **764**, 156–166.

Barrett, T. R., McIntosh, S. C., Fursdon, M., Hancock, D., Timmis, W., Coleman, M., Rieth, M. & Reiser, J. (2015). *Fusion Eng. Des.* **98**–**99**, 1216–1220.

Batra, I. S., Dey, G. K., Kulkarni, U. D. & Banerjee, S. (2003). *Mater. Sci. Eng. A*. **356**, 32–36.

Cackett, A. J. (2020). Size effects in dislocation-mediated plasticity in copper alloys with different microstructural length-scales. Queen Mary University of London.

Cackett, A. J., Lim, J. J. H., Klupś, P., Bushby, A. J. & Hardie, C. D. (2018). *J. Nucl. Mater.* **511**, 610–616.

Cackett, A. J., Vo, H. T., Lim, J. J. H., Bushby, A. J., Hosemann, P. & Hardie, C. D. (2021). *J. Nucl. Mater.* **submitted**,.

Chbihi, A., Sauvage, X. & Blavette, D. (2012). *Acta Mater.* **60**, 4575–4585.

Chen, X., Jiang, F., Jiang, J., Xu, P., Tong, M. & Tang, Z. (2018). *Metals (Basel).* **8**, 227.

Chen, X., Jiang, F., Liu, L., Huang, H. & Shi, Z. (2018). *Mater. Sci. Technol.* **34**, 282–288.

Coenen, J. W., Antusch, S., Aumann, M., Biel, W., Du, J., Engels, J., Heuer, S., Houben, A., Hoeschen, T., Jasper, B., Koch, F., Linke, J., Litnovsky, A., Mao, Y., Neu, R., Pintsuk, G., Riesch, J., Rasinski, M., Reiser, J., Rieth, M., Terra, A., Unterberg, B., Weber, T., Wegener, T., You, J.-H. & Linsmeier, C. (2016). *Phys. Scr.* **T167**, 014002.

Domptail, F., Barrett, T. R., Fursdon, M., Lukenskas, A. & You, J. H. (2020). *Fusion Eng. Des.* **154**, 111497.

Edwards, D. J., Singh, B. N. & Tähtinen, S. (2007). *J. Nucl. Mater.* **367-370 B**, 904–909.

Fursdon, M., Barrett, T., Domptail, F., Evans, L. M., Luzginova, N., Greuner, H., You, J. H., Li, M., Richou, M., Gallay, F. & Visca, E. (2017). *Phys. Scr.* **T170**, 014042.

Greuner, H., Böswirth, B., Barrett, T. R., Crescenzi, F., Gallay, F., Hunger, K., Richou, M., Visca, E., von Müller, A. & You, J. H. (2019). *Fusion Eng. Des.* **146**, 216–219.

Hatakeyama, M., Toyama, T., Nagai, Y., Hasegawa, M., Eldrup, M. & Singh, B. N. (2008). *Mater. Trans.* **49**, 518–521.

Heenan, R. K., Rogers, S. E., Turner, D., Terry, A. E., Treadgold, J. & King, S. M. (2011). *Neutron News*. **22**, 19–21.

Ivanov, A. D., Nikolaev, A. K., Kalinin, G. M. & Rodin, M. E. (2002). *J. Nucl. Mater.* **307**–**311**, 673–676.

Jha, K., Neogy, S., Kumar, S., Singh, R. N. & Dey, G. K. (2021). *J. Nucl. Mater.* **546**,.

Kalinin, G. M., Ivanov, A. D., Obushev, A. N., Rodchenkov, B. S., Rodin, M. E. & Strebkov, Y. S. (2007). *J. Nucl. Mater.* **367**–**370**, 920–924.

Kalinin, G. & Matera, R. (1998). *J. Nucl. Mater.* **258**–**263**, 345–350.

Lukenskas, A., Barrett, T. R. R., Domptail, F., Fursdon, M., Schoofs, F., Greuner, H., Roccella, S., Visca, E., Gallay, F., Richou, M., You, J.-H. H., Domptail, F., Schoofs, F., Greuner, H., Dose, G., Roccella, S., Visca, E., Gallay, F., Richou, M. & You, J.-H. H. (2019). *Fusion Eng. Des.* **146**, 1657–1660.

Mantid Project (2013).

Melnichenko, Y. B. (2016). Small-Angle Scattering from Confined and Interfacial Fluids Springer

International Publishing.
Merola, M., Orsini, A., Visca, E., Libera, S., Moreschi, L. F., Storai, S., Panella, B., Campagnoli, E., Ruscica, G. & Bosco, C. (2002). *J. Nucl. Mater.* **307**–**311**, 677–680.
Park, J.-Y., Lee, J.-S., Choi, B.-K., Hong, B. G. & Jeong, Y. H. (2008). *Fusion Eng. Des.* **83**, 1503–1507.
Schmidt, P. W. (1991). *J. Appl. Crystallogr.* **24**, 414–435.
Teixeira, J. (1988). *J. Appl. Crystallogr.* **21**, 781–785.
Vogel, S. C. (2013). *ISRN Mater. Sci.* 302408.
Xu, X., Odqvist, J., Hornqvist Colliander, M., Thuvander, M., Steuwer, A., Westraadt, J. E., King, S. & Hedstrom, P. (2016). *Metall. Mater. Trans. A*. **47**, 5942–5952.
You, J. H., Visca, E., Barrett, T., Böswirth, B., Crescenzi, F., Domptail, F., Fursdon, M., Gallay, F., Ghidersa, B. E., Greuner, H., Li, M., Müller, A. V., Reiser, J., Richou, M., Roccella, S. & Vorpahl, C. (2018). *Nucl. Mater. Energy*. **16**, 1–11.